machines

MDPI

Article

Investigation of the Aerodynamic Performance of the Miller Cycle from Transparent Engine Experiments and CFD Simulations

Marcellin Perceau [1,2], Philippe Guibert [1], Adrian Clenci [3,*], Victor Iorga-Simăn [4], Mihai Niculae [3] and Stéphane Guilain [2]

[1] Institut Jean le Rond d'Alembert, Sorbonne Université, CNRS UMR 7190, 78210 Saint-Cyr-l'Ecole, France; marcellin.perceau@sorbonne-universite.fr (M.P.); philippe.guibert@sorbonne-universite.fr (P.G.)
[2] Renault, 78280 Guyancourt, France; stephane.guilain@renault.com
[3] Department Automobiles and Transport, University of Pitești, 1, Tg. din Vale Street, 110040 Pitești, Argeș, Romania; mihai.niculae@upit.ro
[4] Regional R&D Center for Materials, Processes and Innovative Products, University of Pitești, 1, Tg. din Vale Street, 110040 Pitești, Argeș, Romania; victor.iorga@upit.ro
* Correspondence: adi.clenci@upit.ro

Abstract: This paper assesses the effect of the Miller cycle upon the internal aerodynamics of a motored transparent spark ignition engine via CFD simulation and particle image velocimetry. Since the transparent Miller engine does not allow for measurements in the roof of the combustion chamber, the extraction of information regarding the aerodynamic phenomena occurring here is based on CFD simulation, i.e., the results of the CFD simulation are used to allow for the extrapolation of the experimental data; thus, they are used to complete the picture regarding the aerodynamic phenomena occurring inside the whole cylinder. The results indicate that implementing the early intake valve closing strategy to obtain the Miller cycle has a negative impact on the mean kinetic energy, turbulent kinetic energy, and fluctuating velocity toward the end of the compression stroke, thus affecting, the combustion process. This supports the need to intensify the internal aerodynamics when applying the Miller cycle such that the turbulence degradation is not too big and, consequently, to still gain efficiency in the Miller cycle.

Keywords: Miller cycle; EIVC; PIV; CFD; RANS; turbulence

check for updates

Citation: Perceau, M.; Guibert, P.; Clenci, A.; Iorga-Simăn, V.; Niculae, M.; Guilain, S. Investigation of the Aerodynamic Performance of the Miller Cycle from Transparent Engine Experiments and CFD Simulations. *Machines* **2022**, *10*, 467. https://doi.org/10.3390/machines10060467

Academic Editors: Davide Astolfi, Chuan Wang, Li Cheng, Qiaorui Si and Bo Hu

Received: 12 April 2022
Accepted: 6 June 2022
Published: 11 June 2022

Publisher's Note: MDPI stays neutral with regard to jurisdictional claims in published maps and institutional affiliations.

Copyright: © 2022 by the authors. Licensee MDPI, Basel, Switzerland. This article is an open access article distributed under the terms and conditions of the Creative Commons Attribution (CC BY) license (https://creativecommons.org/licenses/by/4.0/).

1. Introduction

The knocking and the emission of NO_x in a spark-ignition (SI) engine depend on the pressure and temperature of the gases at the end of compression—in other words, on the volumetric compression ratio—while the thermodynamic efficiency of the SI engine depends in particular on the work provided during the expansion. Consequently, one way to improve the thermodynamic efficiency is to equip the engine with a volumetric expansion ratio that is higher than the volumetric compression ratio. A relatively simple method to achieve different compression and expansion ratios was proposed by Miller [1,2]. The "classic" configuration of the engine is retained, the compression stroke equals the expansion stroke, but the reduction in the volumetric compression ratio is obtained by either early or late intake valves closing (EIVC/LIVC). The valves close either before the arrival of the piston in the bottom dead center (BDC) position, which is followed by an expansion of the air over the rest of the intake stroke, or they remain open during the start of the compression phase and part of the gas admitted is rejected into the intake [2,3]. According to [4], compared with the conventionally throttled Otto cycle, the Miller over-expansion cycle revealed an efficiency improvement of 6.3% in the LIVC mode and of 7% in the EIVC mode. In fact, as stated in the same study, due to its particularities (see above), the Miller cycle can provide a decrease in NO_x emissions of up to 46%.

As shown before, the Miller cycle makes it possible to benefit from an additional rate of expansion, leading to a better thermodynamic efficiency with neither the inconvenience of the risk of knocking nor the aggravation of NO_x emissions. Both aspects are crucial for the future of the SI engine, as the first is directly related to the CO_2 emission, which must be lowered by any means so as to reduce the intensification of the greenhouse effect, whilst the second is associated with pollution and, consequently, with human health [5,6].

Moreover, in the context of the current and future European homologation standards (e.g., Euro6d-full and Euro7), the use of the Miller cycle on SI engines will be one of the preferred choices among the manufacturers [7–9]. After September 2017, as a result of the adoption of homologation in RDE (Real Driving Emissions) conditions [10], it has been imperative to control the engine at lambda 1 over the entire operating range in order to ensure that the best efficiency of the exhaust aftertreatment system is obtained (i.e., maximum depollution). However, operating at lambda 1 under high loads and speeds causes a significant increase in the temperature of the exhaust gases. Usually, before the application of the RDE procedure, the manufacturers enriched the mixture in order to reduce the temperature of the exhaust gases below the limit of the traditional materials used on the exhausts of the vehicles [11]. Obviously, this was done at the cost of pollutants and fuel consumption (i.e., CO_2 emissions). This is no longer possible in the current regulatory context; hence, there is a need to find other solutions to otherwise reduce the exhaust temperature. Due to over-expansion, the use of the Miller cycle also goes in this direction. Therefore, its application determines a significant improvement of the SI engine's efficiency, but it also allows for a significant drop in the temperature of the exhaust gases to the level where it is even possible to use a classic variable geometry turbine (VGT) with further positive effects on fuel efficiency and drivability [12,13]. For instance, on this matter, the research highlighted in paper [8] showed that the low intake charge associated with the EIVC strategy generates a reduced final compression temperature, which permits the compression ratio (i.e., expansion ratio) to be raised to 12.5:1 without encountering extra NO_x emissions or knocking issues and with maximum exhaust temperatures of only 880 °C. Thus, the synergy between the Miller EIVC and VGT was proved. Furthermore, the use of turbocharging is beneficial, as one drawback of the Miller cycle is the reduction of the intake charge/mass generated by the alteration of the valve timing (either the EIVC or LIVC), as shown in [4]. In other words, turbocharging may compensate for the inherent power reduction of the Miller engine compared with a standard SI engine based on the Otto cycle.

Another significant downside of the EIVC Miller cycle is that it strongly affects the internal aerodynamics, which are paramount for the air-fuel mixing and the flame propagation velocity. Indeed, considering the EIVC case, because of a reduced opening time, the tumble motion specific to the SI engine is disturbed, thus having a negative impact on the turbulent kinetic energy later on in the compression stroke [14]. The results of the experimental investigation presented in paper [3] also support the previous statement: the turbulent kinetic energy is reduced to almost zero toward the end of the compression stroke before producing the spark, finally leading to inefficient combustion. In fact, these studies [3,14], underline that the Miller cycle is capable of improvements in the matter of efficiency, but the EIVC strategy has a strong influence on the engine flow field [3], which may need further improvements, such as intake valve masking, intake valve seat masking, or specially-designed intake ducts for a higher tumble, as studied by Niculae et al. [15]. In other words, to gain efficiency, the turbulence degradation inherent to the Miller cycle must not be too high. However, as argued in [14], the EIVC drawbacks regarding the reduced turbulence intensity may be advantageous at high loads and at lower and medium engine speeds for the best fuel efficiency potential and CO_2 reduction potential.

Regarding the implementation of the Miller cycle, both versions can be found on the market. Some manufacturers prefer to implement the EIVC version, while some prefer the LIVC version and others implement both, depending on the engine operating point. For example, in [7], the EIVC strategy was used due to the best fuel efficiency results that

can be achieved in the partial-load area with a combination between the early closing and the large overlap of the intake/exhaust valves. Additionally, the EIVC offers advantages concerning the knock conditions for the supercharged engines. Moreover, as presented in paper [16], the turbulence inside the cylinder at the end of the compression stroke under the EIVC strategy is higher than the turbulence achieved with the LIVC strategy.

The aim of this study is to assess the effect of the Miller cycle upon the internal aerodynamics of a motored/driven SI engine via particle image velocimetry (PIV) and 3D computational fluid dynamics (CFD) investigations. Relating to the PIV results, the transparent engine does not allow for measurements in the roof of the combustion chamber (i.e., this one is unobservable). Only the inside of the transparent cylinder is accessible. Consequently, the extraction of information regarding the aerodynamic phenomena occurring in the upper part of the cylinder when approaching the top dead center (TDC) position was impossible. Since this piece of information is crucial for the flame propagation occurring around the TDC position, to estimate the lacking information, CFD simulation was used as a complementary investigation tool. In other words, the results of the 3D CFD numerical simulation were used to allow for the extrapolation of the data gathered through the PIV investigation and, finally, to complete the picture regarding the aerodynamic phenomena occurring inside the cylinder for a Miller SI engine.

Thus, after this introduction outlining the study in the current context, the remaining part of the paper is organized into three main sections: Section 2 presents the PIV investigation focused on gathering data about the internal aerodynamics of the engine during the intake and the compression strokes, Section 3 shows the CFD approach as a tool to allow for the estimation of aerodynamic phenomena in the region where the PIV is no longer able to provide information, and Section 4 deals with the results and a discussion. Finally, the conclusions of this study are summarized.

2. Experimental Setup

As already introduced, the internal aerodynamics of a Miller cycle SI engine based on the EIVC strategy was first studied experimentally via the PIV technique, which is presented below.

2.1. Model Engine

The model engine was representative of a 0.9 L three-cylinder SI engine for passenger cars and is used solely for non-combustion cycle studies. It was made of a single transparent cylinder offering wide optical access to study the aerodynamic movements inside the combustion chamber. The cylinder head contains four valves—two for the intake and two for the exhaust—in a pent-roof geometry. The engine has a 12.3 compression ratio, an 81.2 mm stroke, and a 72.2 mm bore. A flat piston head was used because a real piston head shape can induce distortions in the laser sheet that could lead to inaccurate positioning and reflections. The cylinder head–piston distance has been changed to maintain the reference compression ratio value, as explained in [17]. Obviously, since the real piston is not used, the internal aerodynamics of the original engine are not fully replicated in the transparent engine. In other words, the effect of the real piston is not captured; yet, it may be assumed that it has a low influence.

All the measurements were made with the engine driven at 1200 rpm by an electric motor and at an intake pressure of 1 bar. Since the engine has a glass cylinder without lubrication, this relatively low speed was chosen in order to avoid damaging it.

The PIV experiments were performed in the tumble plane, which passes through the axis of the cylinder and the middle of the two intake and exhaust valves (Figure 1).

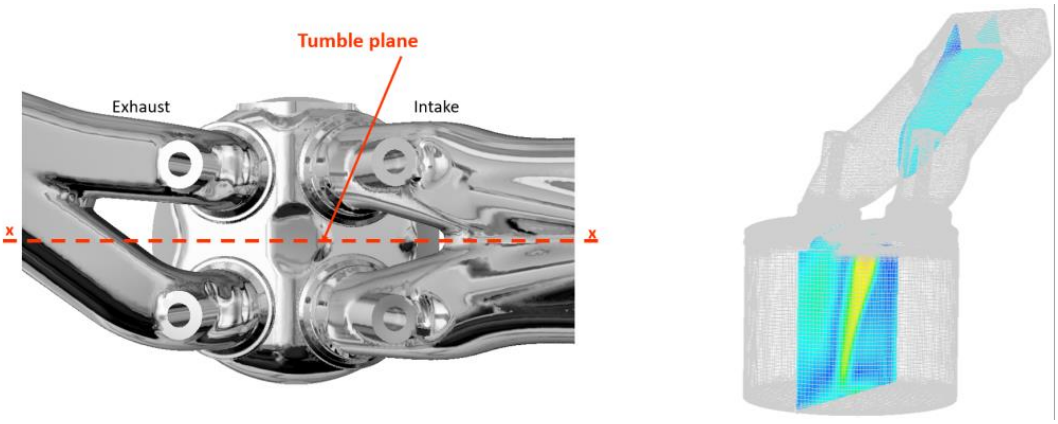


Figure 1. The tumble plane investigated with the particle image velocimetry (PIV).

Figure 2 comparatively illustrates the valve lift laws for the Miller case (the dashed curves) and for the Otto case (the continuous curves). Thus, it can be observed that the transparent engine followed an EIVC Miller cycle. In fact, to highlight the influence of an earlier intake valve closing, two Miller cases were used in this study: one characterized by a 30° CA offset at the intake camshaft (see the curve represented with long blue dashes) and the other by a 20° CA offset (see the curve represented with small blue dashes). These two intake valve lift laws were coupled with the following exhaust offsets: 0° CA and 30° CA (see the curves represented with small and long red dashes). Both cases were possible thanks to a variable valve timing (VVT) system. The intake valve opening duration measured for a reference lift of 0.7 mm is 140° CA in the Miller case and 160° CA in the Otto case. The original engine is meant to operate following the Otto cycle only in the full load condition.

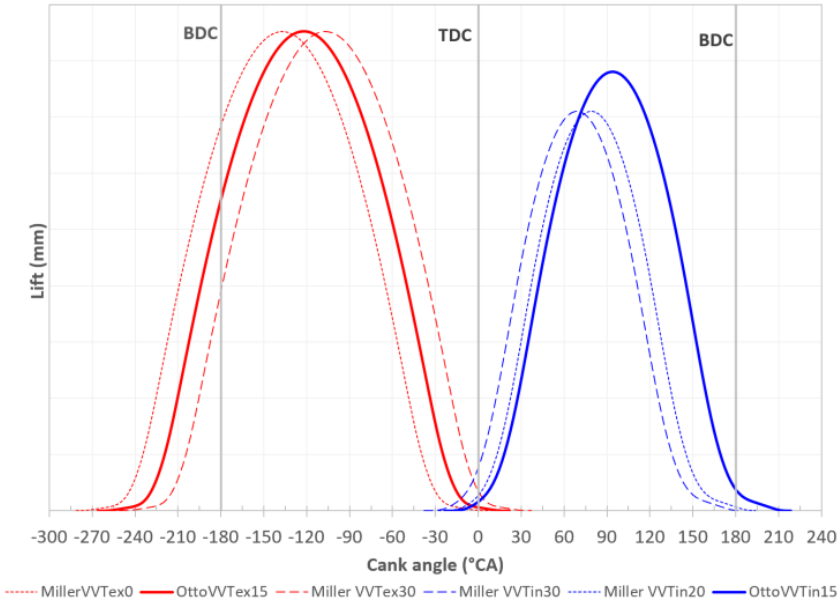


Figure 2. Exhaust and intake events: valve lift laws.

2.2. Particle Image Velocimetry Measurements

There are several types of PIV technologies that can be used on optically accessible engines. For example, the PIV system used by the Institute of Aerodynamics from RWTH Aachen University is a high-speed stereo PIV [18]. This system is used to study the internal aerodynamics of an externally driven (1500 rpm) optical Miller cycle engine. The laser light

sheet is directed into the cylinder using a 45° mirror. The measurements are conducted at a temporal resolution of 0.1° CA.

Another example of a high-speed PIV system used with the Miller cycle was at the Institute of Technology of Tokyo [19]. This study was conducted on an optically accessible engine driven at 2000 rpm. The PIV was performed at 12 kHz with the following characteristics: a resolution of 1° CA; tracer particles with a diameter between 2–2.5 µm illuminated with a laser with a maximum power of 50 W and a wavelength of 532 nm; a laser pulse width of 200 ns; a laser sheet thickness of 313 µm at the bore center.

The PIV system, available at Darmstadt University and used for optical measurements, is a Tomographic PIV applied for a motored single-cylinder engine driven at 800 rpm [20]. In this case, the PIV system is equipped with four cameras in a "Scheimpflug" arrangement in a circular plane around the cylinder. The laser light sheet is also directed into the cylinder using a 45° mirror.

Another type available at the same institute is the Thermographic PIV, which uses luminous phosphor particles to trace the fluid motion, these particles also being used for the measurement of the particles' temperature [21].

Certainly there are other types of PIV systems such as micro PIV, holographic PIV, tomographic PIV [22], scanning PIV [23], laser speckle velocimetry [24], molecular tagging velocimetry [25], or laser doppler velocimetry [26], each one with advantages and drawbacks.

In our case, the in-cylinder flow was seeded with oil particles. An aerosol generator produced particles of approximately 1–10 µm at a concentration of more than 108 particles per cm^3. These particles were then illuminated using a light sheet with a thickness of less than 1 mm. Light was emitted from a double pulsed Nd-YAG laser (Specta Physics PIV 200) at a wavelength of 532 nm. The separation time between the two laser pulses was 15µs. The maximum output energy was around 200 mJ per pulse, with a pulse duration in the range of 8–10 ns. This laser provided a stable cycle-to-cycle illumination of the transparent cylinder at a $10^{\pm 2}$ Hz frequency (Figure 3), which means that one velocity field is recorded for every engine cycle at the same crank angle. After going through a Nikon AF Nikkor 50 mm f/1.8D, the scattered light was captured on a monochrome charge-coupled device camera (Jai CV-M2 CL) with a resolution of 1600 × 1200 pixels.

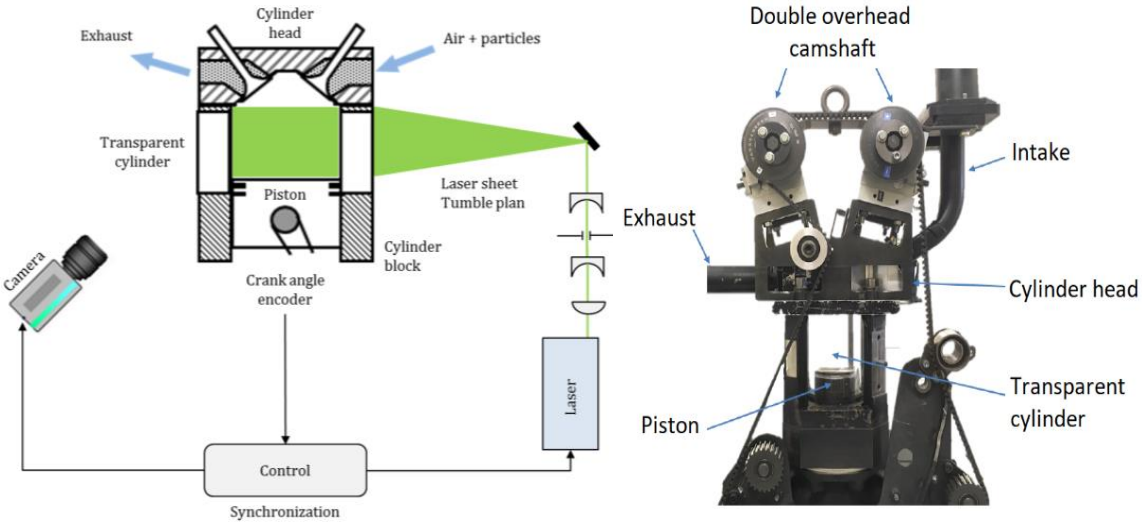


Figure 3. Particle image velocimetry (PIV) measuring system and transparent engine.

The synchronization of these devices was performed using a controller that took the signal of the engine crank angle encoder as the input. For a given crank angle, the measurement began after the rotation speed of the engine was stable. It then took 300 pairs of images corresponding to 300 engine cycles at the desired crank angle, which were used to obtain the average flow field, as shown in Section 4.1. This procedure was repeated

for any other crank angle for which the flow fields are desired, meaning that the engine is switched off before recording another crank angle. An adaptive cross-correlation PIV algorithm from Dantec Dynamic Studio v6.8 software is used to process the pairs of images. The interrogation area went from 32 × 32 to 64 × 64 pixels according to the particle density, and a grid step size of 16 × 16 pixels was used. For each instantaneous velocity field, 76 × 61 instantaneous velocity vectors were finally provided, with a spatial resolution of about 2 mm.

3. Numerical Investigations

As already stated, this purpose of the CFD investigation is to provide data for the extrapolation of the PIV results toward the end of the compression. The CFD investigation is a 3D RANS-based (Reynold-average Navier–Stokes) cold simulation of the transparent single-cylinder Miller cycle engine motored at 1200 rpm. The simulation is termed cold because the engine is not fired. The CFD investigation was performed using the AVL Fire™ 2022 R1 software (Graz, Austria), which is based on the finite volume approach. Additionally, the *k-ζ-f* turbulence model was used [27,28].

3.1. Reynolod-Average Navier–Stokes Formalism and Turbulence Model

The movement of the air inside the cylinder during the intake and the compression strokes or the internal aerodynamics of an engine are very important factors in the combustion process. Internal aerodynamics play a major role in volumetric efficiency, the heat exchange with cylinder walls, the homogenization of fresh mixture, and, finally, chemical reactions during combustion, which depend on the characteristics of the transport and turbulent diffusion.

Navier–Stokes equations are used to describe the fluid dynamics as laminar or turbulent. They are non-linear, second-order partial differential equations without exact solutions. From an engineering standpoint, sometimes only the averaged mean velocity fields are looked for (e.g., the fluid–structure interaction). Consequently, for these reasons, the CFD methods consider the statistically averaged equations derived from the principle of Reynolds decomposition, i.e., RANS. This approach is about decomposing the flow properties into an average value and a fluctuation component, which gives rise to a new, unknown Reynold-stress tensor that has to be modeled in order to solve the rest of the equations [29]. The RANS model offers a good balance between the duration of the simulation, the accuracy of the results, and cost effectiveness. The RANS model is usually used to predict the engine in-cylinder mean flow and turbulence distribution since it is good enough to capture the overall qualitative flow trends [30]. This is also supported by studies [31,32] that highlight the fact that CFD simulation using the RANS approach is an efficient and reliable tool for the fluid flow of the internal combustion (IC) engine. Nevertheless, the approach is limited for unsteady flows, while the hybrid models such as the large eddy simulation (LES) or unsteady Reynolds-averaged Navier–Stokes (URANS) provide a better prediction of smaller fluctuations. However, hybrid models require higher numerical schemes, smaller time steps, and higher resolutions for the computational grids. Therefore, the RANS approach can be used to save processing power (CPU) and reduce the simulation time, depending on the type of research.

According to [33], choosing a suitable turbulence model for IC engines is an unresolved issue in the scientific community. It is argued that most turbulence models are validated for specific well-defined test cases, but it is not certain that they are also valid for other type of flows generated by complex geometries where the flow might be different. The models used in [33] were: LES (Smagorinsky, WALE, Sigma), the hybrid model, and the second generation of unsteady Reynolds-averaged Navier–Stokes (URANS). The results indicated that LES with the Sigma turbulence model is suitable for IC engine flow and, compared with other hybrid models, highlights a higher number of resolved turbulent structures. Nevertheless, for most of the cases, the URANS approach offered reasonable results to describe the fluid flow for higher engine speeds and a higher Reynolds number [33]. On the

other hand, as discussed in [34], most URANS models are poor in recreating the swirling flow in steady-flow configurations, while the LES model offers better results. Nonetheless, as mentioned in [35,36], LES applications are not straightforward due to the need for specific boundary conditions and severe grid resolutions/quality compared to RANS. In fact, as seen in the scientific literature, there are many methods and approaches already available, but none of them are suitable for every situation.

In terms of the turbulence models that can be used with the RANS approach, there are several such examples, each with its own advantages and disadvantages. For example, the *k*-ε model is simple to implement, leads to stable calculations, and is reasonably accurate for a variety of flows, but it is only valid for fully turbulent flows, predicts the swirling and rotating flows rather poorly, and comes down to a simplistic ε equation. The *k*-ω model solves two additional partial differential equations, but it suffers from similar drawbacks as the *k*-ε model. The Reynolds stress model (RSM) has a good accuracy in predicting complex flows such as swirling flows, rotating flows, or flows that involve separation, but it requires double or even triple the processing power in order to perform the numerical simulation [37].

In order to obtain a smoother scaling, especially near solid walls, the *k*-*g* model can be used, where *g* represents the square root of a characteristic turbulent time scale [38,39]:

$$g = \sqrt{\frac{k}{\varepsilon}}, \tag{1}$$

As shown in [38], this model reveals good and consistent results for steady intake jet flows in the IC engine, while for more complex reciprocating flows, the results are mixed.

Another turbulence model used, similar to the *k*-ε model, is *k*-ζ-*f*, which provides a good balance between computational cost and the accuracy of the results due to the particularities of the ζ term modeling [40]. According to [40], both RANS with RSM and the *k*-ζ-*f* model produce reasonable results with a good accuracy in resolving the dominant structures of the turbulent flow. In comparison with LES, the *k*-ζ-*f* model has a better advantage in managing computational cost efficiency, even compared with the RSM, which it is 20% faster than. Regarding the two RANS models, paper [40] showed that the *k*-ζ-*f* model provides a better prediction of flow separation and reattachment. The *k*-ζ-*f* model has been developed by Hanjalic, Popovac and Hadziabdic [27]. The authors propose a version of the eddy viscosity (ζ) model based on Durbin's elliptic relaxation concept, *f* [41]. As stated in [27,28], the aim was to improve the numerical stability of the original $v2 - f$ model, which had become increasingly popular as empirical damping functions were removed due to the employment of an additional velocity scale $v2$ derived by using an elliptic relaxation concept (f). As argued in [42], "the four-equation *k*-ζ-*f* model is very robust and more accurate than the simpler two equation eddy viscosity models. On average, the computing time is increased by up to 15% compared with the computing time needed for the *k*-ε model calculations". Nevertheless, as stated in [42], "the model is usable for a relatively coarse mesh next to the wall, but the cell next to the wall should reach a non-dimensional wall distance y^+ of 3 as a maximum". Moreover, as reported in the same publication [42], "the flow in an intake port shows good agreement between computed and measured discharge coefficient". Equally, one particular advantage is that it is sufficiently robust to be used for computations involving grids with moving boundaries and highly compressed flows, as is the case in IC engines.

In light of the above considerations, the *k*-ζ-*f* turbulence model with a maximum cell size of 1.0 mm was chosen for our CFD simulation.

3.2. Simulation Description

The 3D geometry of the engine can be seen in Figure 4, which also presents the positions of the sensors used to continuously monitor the inlet and outlet pressures, as well as the in-cylinder pressure. The first two signals (Figure 5) were used to impose the

boundary conditions (BC), while the in-cylinder pressure signal served to provide a mean for comparison with the result of the CFD simulation.

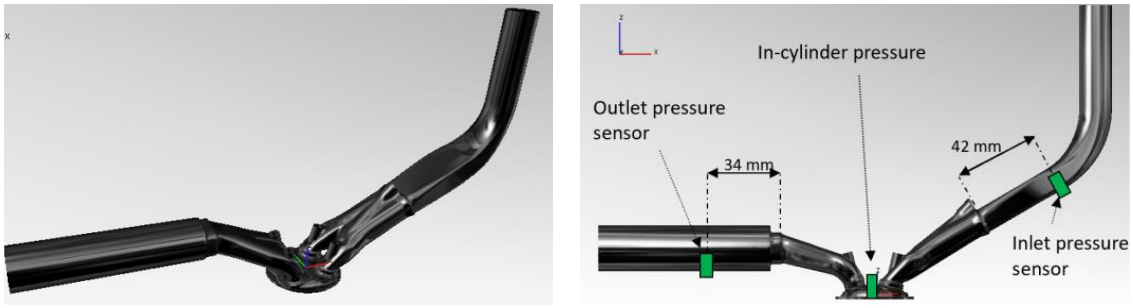


Figure 4. 3D engine geometry.

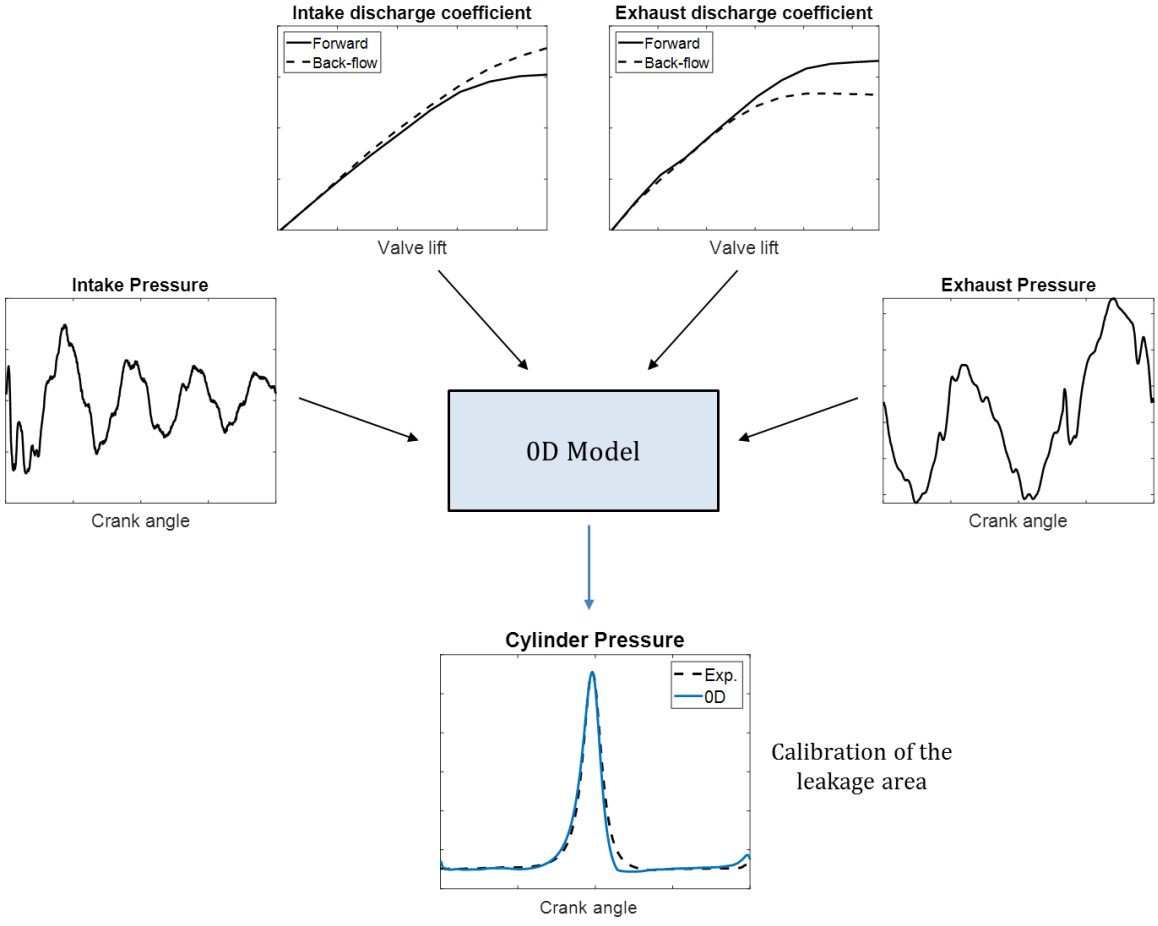


Figure 5. 0D modeling of the transparent engine—blow-by rate estimation.

By design, the transparent engine has a higher leakage rate between the piston and the cylinder liner than a conventional engine does. This is because the rings, which are partly made of graphite and vespel (polyimide-based plastics), do not scrape the cylinder walls as hard as conventional metal rings. Therefore, they allowed the engine to be sealed without damaging the transparent cylinder.

To be able to simulate the real phenomena occurring in the transparent engine, the blow-by flow mass rate must be estimated so that the numerical 3D model and the transparent engine can have a similar behavior (i.e., the same air mass trapped in the cylinder). In other words, the blow-by flow mass rate must be imposed as a boundary condition in the 3D CFD model.

As shown in Figure 5, the estimation of the blow-by flow mass rate is accomplished via 0D modeling, and, finally, the result is validated by comparing the pressure curve given by the 0D model [43] to the one experimentally read on the transparent motor.

This model takes the intake and exhaust pressure signals as boundary conditions, and it also considers the pressure drops at the valves of the transparent engine. The superposition of the two pressure curves is done by calibrating the leakage section, A_{bb}, and the theoretical blow-by flow rate, $\dot{m}_{th}$, is modeled similarly to the flow through valves in the usual way [44]. The value of the leakage section is taken differently depending on the value of the internal pressure in the cylinder. Indeed, the rings do not have the same behavior when the flow is incoming or outgoing:

$$A_{bb} = \begin{cases} A_{bb,\,sup} \; if \; P_{cyl} > P_{atm} \\ A_{bb,\,inf} \; if \; P_{cyl} < P_{atm} \end{cases}, \tag{2}$$

where $A_{bb,\,x} = \pi\left(D_{cyl}^2 - \left(D_{cyl} - 2gap_x\right)^2\right)/4$ with $gap_{sup} = 0.0657$ mm and $gap_{inf} = 0.66$ mm (for the case of the $VVT_{intake/exhaust} = 20/00°$ CA valve timing). The value gap_{sup} is used to calibrate the maximum pressure given by the model, and that of gap_{inf} is adjusted to have an admitted air flow rate estimated by the model that is equal to that observed experimentally. To have an idea of the order of magnitude of the leakage, the gap_{sup} creates an equivalent leakage surface of a circular section with a diameter of 4.35 mm, as shown in Figure 6.

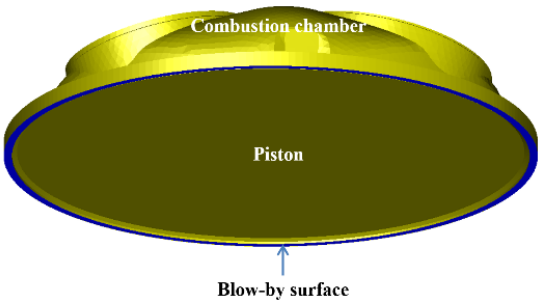
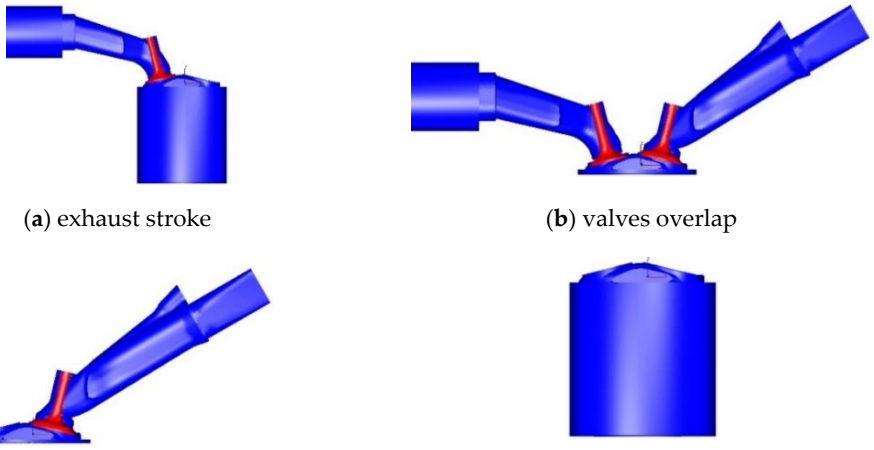


Figure 6. Imposing the blow-by flow rate as a boundary condition.

With respect to the geometry presented in Figure 4, the computational domain was slightly reduced because, as seen in Figure 7, the geometry beyond the areas corresponding to the inlet and outlet pressure sensors was not maintained (i.e., the computational domain starts and ends with the areas where the BCs are imposed).



(**a**) exhaust stroke (**b**) valves overlap

(**c**) intake stroke (**d**) compression and expansion strokes

Figure 7. The computational domain.

To maintain the computational time within reasonable limits, on the one hand, the chosen timestep of the simulation was 1° CA, and, on the other hand, various grid zones were successively enabled and disabled according to the engine's physical strokes. In other words, during the calculation, the computational domain is divided into three main parts, and two of those parts, the intake and exhaust ones, are successively enabled/disabled depending on the simulation time (Figure 7):

- the exhaust duct, the exhaust ports, and the cylinder → exhaust stroke (Figure 7a);
- the exhaust, the cylinder, and the intake → valves overlap (Figure 7b);
- the intake duct, the intake ports, and the cylinder → intake stroke (Figure 7c);
- the cylinder → compression and power/expansion stroke (Figure 7d).

The discretization is created through the pre-processing software included in the AVL Fire, namely, the Fame Engine Plus module (FEP), which is an automatization used to set up a moving and deformable mesh engine project.

The turbulence model used for this application is of the high-Reynolds numbers type, which means it is not applicable in the near-wall region. In order to model the near-wall effects, the hybrid wall function was set, which was meant to ensure a gradual change between the viscous sublayer and the wall function. This hybrid wall function, which, as mentioned in [42], is recommended for use in conjunction with the k-ζ-f turbulence model, is actually a proprietary semi-empirical-based fitting function between the laminar and the turbulent part of the boundary layer obtained from experimental evidence. Therefore, the chosen wall treatment was an automatic one. Thus, the CFD code evaluated the y^+ (the usual dimensionless wall normal distance utilized in the boundary layer problem) and then selected the appropriate wall function on the fly without any user input. Hence, the computational domain was meshed automatically with a greater refinement in the areas susceptible to very high flow velocities such as the valve gaps, where the y^+ value is below 3 in the low lift periods, as can be seen from Figure 8.

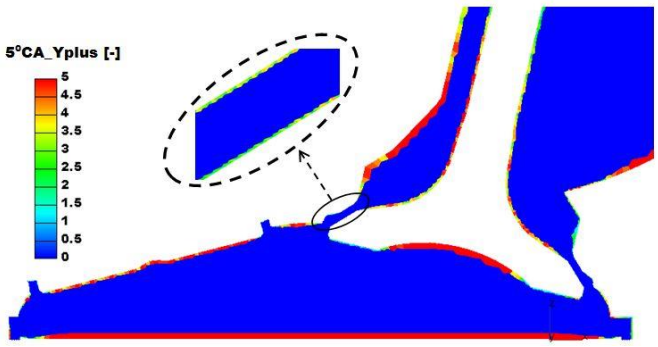


Figure 8. The y^+ dimensionless wall normal distance at the intake valve gap.

The details of the resulting mesh are given in Table 1, and an image of the meshed geometry is provided in Figure 9.

Table 1. Details of the geometry mesh.

Max. Cell Size	Max. Number of Cells	Repartition	(%)	Min. Number of Cells	Repartition	(%)
1 mm	7,527,028 (@180° CA)	hexahedral	82	2,866,060 (@360° CA)	hexahedral	81.5
		tetrahedral	0.67		tetrahedral	1.01
		prismatic	10.5		prismatic	13.89
		pyramidal	5.92		pyramidal	7.9

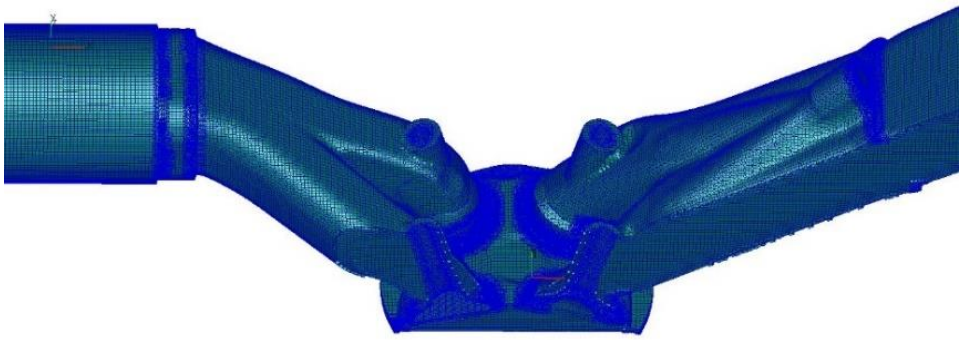


Figure 9. The meshed geometry.

As seen from Table 1, the predominant cell shape is hexahedral, but tetrahedral, prismatic, and pyramidal cells were also used for the areas with specific and complicated geometries. As the mesh is a moving and deformable one, the number of cells varies from 7,527,028 at the start of the intake stroke (Figure 7b) to 2,866,060 at the end of the compression stroke. To analyze the influence of the grid upon the numerical solution, different values for the maximum cell size were used (1.3, 1.0, and 0.7 mm). Obviously, this has a direct influence on the meshing and computational time of our Intel Xeon machine (2.3 GHz, 36-core processor, and 128 GB of RAM), as shown in Table 2.

Table 2. Computational time for one complete cold engine cycle.

Max. Cell Size [mm]	**1.3**	**1.0**	**0.7**
Meshing time [hours]	9	17	27
Simulation time [hours]	19	96	185

Since further decreasing the maximum cell size from 1.0 mm to 0.7 mm did not result in an obvious improvement (no apparent change in the large-scale structures), the maximum cell size used for the CFD study was 1.0 mm.

4. Results

This section focuses on comparing the experimental results with those obtained by the numerical CFD simulation. It starts by comparing the mean flows generated by the two Miller intake valve lift laws presented in Figure 2 and then ends by comparing the turbulence generated when using these two cases.

Obviously, this kind of methodology is typical for the flow studies. One could even say it has always been privileged because the two approaches (experimental and numerical) are complementary, as will be shown subsequently.

Thus, in order to obtain information about the internal aerodynamics of the engine at the end of the compression stroke, in the combustion chamber, which is not observable for the PIV investigation, our method relied on estimating these missing data with the help of the CFD results. More precisely, since both approaches (CFD and PIV) offered comparable trends for the mean kinetic energy and fluctuating velocity, the results of the 3D CFD numerical simulation were used to allow for the extrapolation of the data gathered through the PIV investigation and, finally, to complete the picture regarding the evolution of the aerodynamic phenomena occurring inside the cylinder for a Miller SI engine featuring two VVT offsets.

Therefore, this paper also aims to highlight that, despite the differences generated by the comparison between the experimental and the numerical results, useful conclusions may still be drawn because both approaches (CFD and PIV) offered comparable trends.

4.1. Mean Flow

Figures 10 and 11 present a side-by-side comparison of the average flow fields generated by the two Miller cases presented in Figure 2 ($VVT_{in/ex}$ = 20/00° CA and $VVT_{in/ex}$ = 30/30° CA). In these pictures, the intake valves are on the right. On the PIV results, the circled blue areas from the upper right corners and from the low left side are the effect of some reflections which could not be suppressed. Moreover, concerning the stair shape from the bottom of the PIV flow fields at 270° CA and 320° CA, this is because the piston blocks the laser sheet, and the closer it gets to TDC, the more accentuated this effect is.

When analyzing Figures 10 and 11, even though there are common features, one can first observe that the shapes of the structures are not identical between the numerical and experimental results.

Indeed, especially at 200° CA, there are noticeable differences in the large-scale structures between the two approaches (CFD and PIV). For this position, the CFD predicted a large-scale structure which is not characterized by a single center of rotation, as the PIV revealed. One may also notice a rotational flow around an elongated upper area (see the white curve from Figures 10 and 11). Despite these initial differences, at 270° CA, the large-scale flow fields may be considered close enough. Both approaches showed centers of rotation situated in the upper left regions (see the small white dots from Figures 10 and 11) with respect to the previous angular position. As for the 320° CA, ignoring the regions pointed out in Figures 10 and 11 with small vertical ellipses, which can be explained by a slight deposit of dust on the inner surface of the cylinder responsible for some reflections, once again, the large-scale flow fields featuring centers of rotations displaced even more to the upper left region with respect to the previous position may be considered comparable.

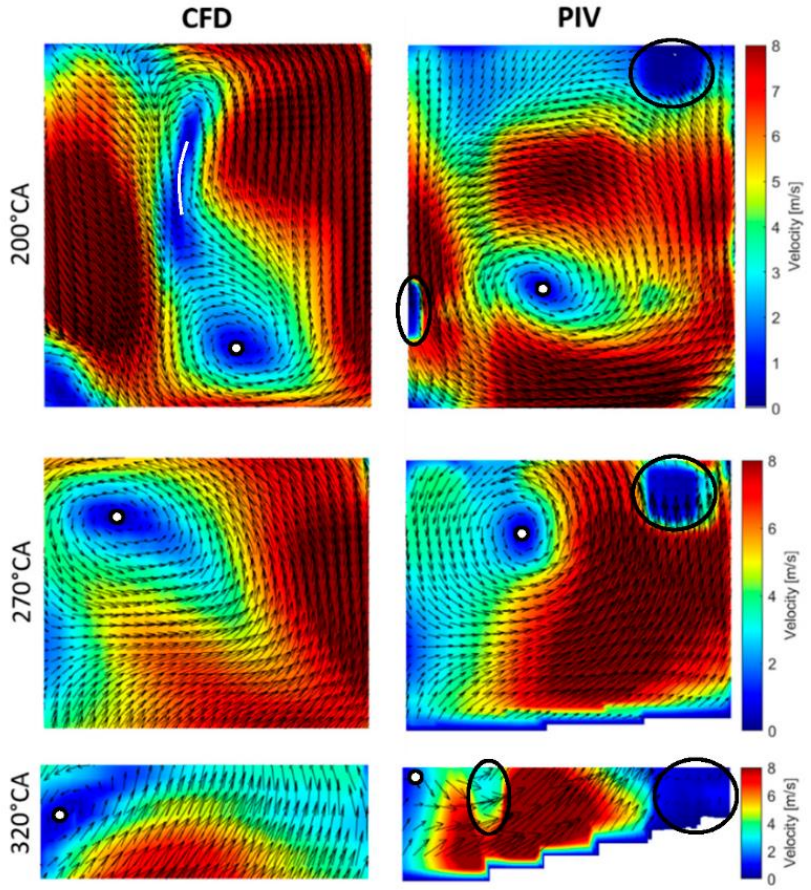


Figure 10. Mean flow velocity fields: simulation (**left**) and experiment (**right**)—$VVT_{in/ex}$ = 20/00.

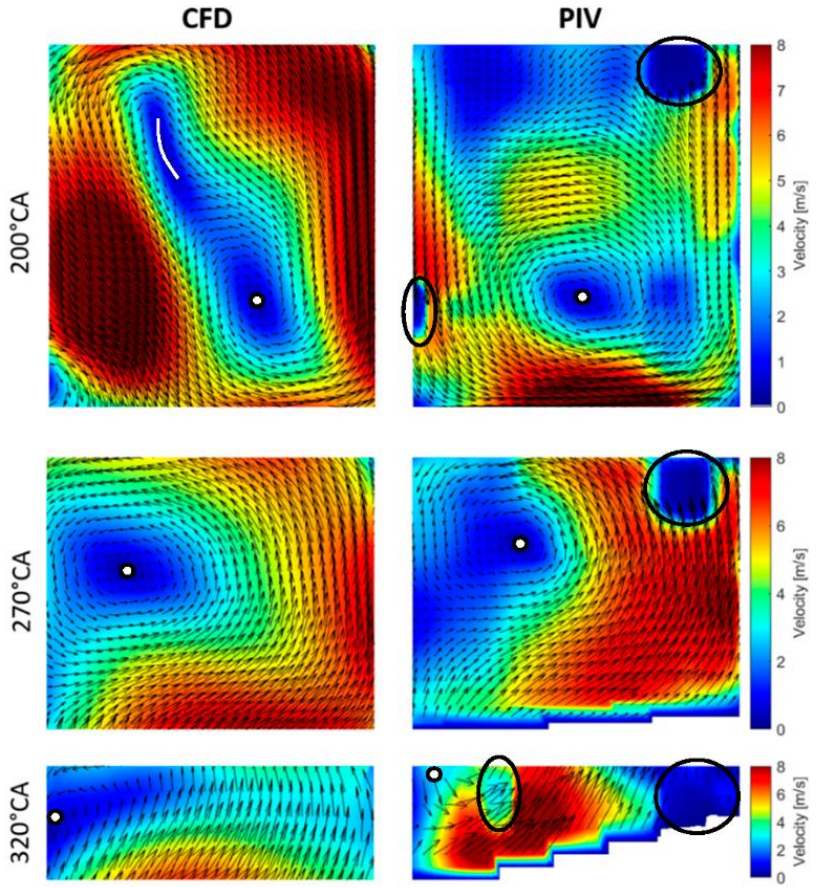


Figure 11. Mean flow velocity fields: simulation (**left**) and experiment (**right**) $VVT_{in/ex}$ = 30/30.

For all of the angular positions, the order of magnitude of the measured vs. simulated velocities is the same.

It is also interesting to notice from both data sets, CFD and PIV, that the effect of closing the intake valves earlier ($VVT_{in/ex}$ = 30/30) leads to a decrease in the intensity of the air movement.

Regarding the differences between the CFD prediction and the PIV reality, one reason could be related to a blow-by flow mass estimation not in full concordance with reality. This being set in the simulation as a boundary condition has a direct influence upon the numerical results. Another reason could be connected to the RANS model constants generally used for IC engine flow predictions, which were taken from the classical Otto cycle. Moreover, on the method of calculation of the average flow field, the RANS result is not the same average as the average of the PIV. An identical methodological approach would lead us to use the LES on as many cycles as possible so that the average was statistically converged. In the experiments, despite all the precision brought to the measurements, a discrepancy could be explained by a slight/inherent mechanical dissymmetry of the lift of the two intake valves, which would then generate a tumble plane not symmetrical to the direction of the flow. Furthermore, the particles seeded in the in-cylinder flow were then illuminated using a light sheet with a thickness of about 1 mm.

However, despite these differences, as will be shown subsequently, the trends illustrated by the two approaches (CFD and PIV) may be considered as close enough, which supports the idea of estimating the missing PIV data corresponding to the end of the compression stroke with the help of the CFD results, as already mentioned.

To quantify the difference between the velocity fields shown in Figures 10 and 11, the choice was made to calculate the mean kinetic energy (*MKE*) based on the velocities of the 2*D* grid's nodes going from 1 to N_m:

$$MKE_{2D} = \frac{1}{N_m} \sum_{k=1}^{N_m} \frac{U_k^2 + V_k^2}{2} \tag{3}$$

Figure 12 shows the result of the calculation for the two VVT offsets.

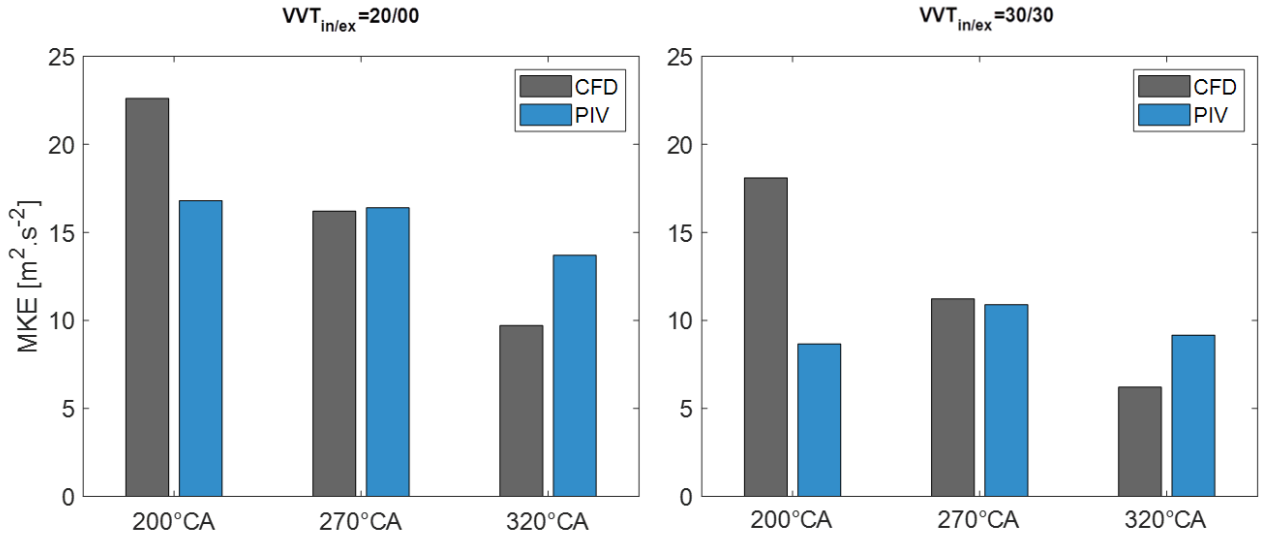


Figure 12. Comparison of the 2D mean kinetic energy: simulation vs. experiment.

As shown in Figure 12, the MKE differences observed at the beginning of the compression stroke (200° CA) are greatly reduced at mid-compression (270° CA). The values are then slightly different at the end of the compression (320° CA). Nonetheless, at least the differences are in the same way (at the PIV, lower at 200° CA and higher at 320° CA). An explanation for these differences could be the smaller vector number provided by the PIV measurements compared to the CFD measurements.

4.2. Turbulent Flow

The turbulence model of the CFD software can estimate the turbulent kinetic energy (TKE) during the engine cycle. This quantity, named *k*, corresponds to the temporal average of the kinetic energy per unit of mass associated with the turbulent flow. It is written as follows:

$$k_{CFD} = \frac{1}{2}\left(\overline{(u_1')^2} + \overline{(u_2')^2} + \overline{(u_3')^2}\right) \tag{4}$$

where $\overline{X}$ represents the temporal average of the quantity *X* and corresponds to the average during the engine cycles for the CFD data.

It is therefore necessary to calculate *k* from the PIV data. The turbulence model is based on the Reynolds decomposition. It will then be used to extract the fluctuations of the component *i* of the velocity fields:

$$u_i' = u_i - \overline{u}_i \tag{5}$$

A problem appears when comparing the CFD and PIV data. The PIV measurement is plane and thus gives access to only two components of the velocity. The turbulent kinetic

energy will consequently be theoretically lower than the one calculated from the CFD model (apart from any other consideration):

$$k_{PIV_2D} = \frac{1}{2}\left(\overline{(u_1')^2} + \overline{(u_2')^2}\right) \tag{6}$$

However, this difference can be minimized. Indeed, the turbulence model is based on the assumption of the isotropy of the turbulence, i.e., the fluctuations are similar in all directions $\left(\overline{(u_1')^2} = \overline{(u_2')^2} = \overline{(u_3')^2}\right)$. A second expression of the TKE can then be used for the PIV data by estimating the contribution of the third component as follows:

$$\overline{(u_3')^2} = \frac{\overline{(u_1')^2} + \overline{(u_2')^2}}{2} \tag{7}$$

The TKE from the PIV data, under the assumption of isotropic turbulence, is then written:

$$k_{PIV,\,iso} = \frac{1}{2}\left(\overline{(u_1')^2} + \overline{(u_2')^2} + \frac{\overline{(u_1')^2} + \overline{(u_2')^2}}{2}\right) \tag{8}$$

This assumption of isotropy also allows for the definition of a quantity u' to quantify the fluctuations, which is calculated as the average of the fluctuations in the three directions:

$$u' \equiv \sqrt{\frac{1}{3}\left(\overline{(u_1')^2} + \overline{(u_2')^2} + \overline{(u_3')^2}\right)} = \sqrt{\frac{2}{3}k} \tag{9}$$

Note that in the results presented later, k and u_0 are calculated at each point of the measurement plane in both cases (CFD/PIV). The spatial average of this set is then calculated to obtain values of TKE and fluctuating velocity at a specific time.

To estimate the order of magnitude of the TKE before combustion, the two CFD calculations for the two VVT offsets were performed in the transparent engine configuration. The mean value of the TKE and, therefore, u' was then extracted in the tumble plane at different crank angles.

As shown in Figure 13, which is about a trend predicted based on discrete crank angular positions, the results between CFD and PIV were compared at the same crank angles as before (200, 270, and 320° CA). Then, the TKE (i.e., u') values given by the CFD at the angles 340 and 355° CA were used to extrapolate those of the PIV to estimate the turbulence generated in the transparent engine configuration near TDC. The dashed curve, corresponding to the extrapolated PIV values, is calculated by shifting the CFD values by the offset k_{CFD} (320° CA) − k_{PIV} (320° CA). Note that the TKE of the PIV values is calculated under the assumption of turbulence isotropy. The left-hand side of Figure 13 shows the results for the $VVT_{in/ex}$ = 20/00° CA offset. The shape of the curves follows the same trend in both cases. The maximum TKE at 340° CA of the extrapolated PIV values is 9.44 $m^2\ s^{-2}$, which gives a turbulent velocity of 2.35 m s^{-1}.The right-hand side of Figure 13 presents the results of the $VVT_{in/ex}$ = 30/30° CA offset, with a maximum TKE of 7.24 $m^2\ s^{-2}$ and a velocity of 2.07 m s^{-1}. The curves appear less comparable. However, the expected effect of an advance of the closing time of the intake valves (VVT_{in} going from 20 to 30° CA) on the TKE is verified. This advance of closing decreases the order of magnitude of the TKE before combustion. These findings are also concordant with the results shown in [3,14].

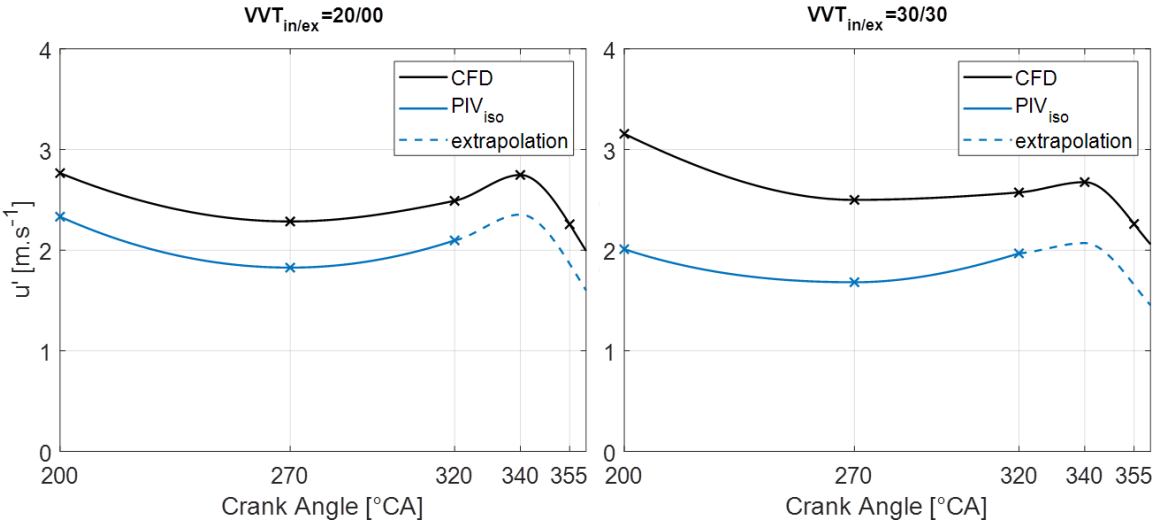


Figure 13. Comparison of the fluctuating velocities between the simulation and experiment.

These values of the fluctuating velocity are low. The values found by the PIV in the tumble plane, in a previous study with the same configuration but following an Otto cycle [17], were of the order of 3.5 m s $^{-1}$ at 330° CA. This further demonstrates the importance of intensifying the internal aerodynamics when applying the Miller cycle, as shown in paper [15].

Similar evolutions of the fluctuating velocities can also be found in paper [43], which provided an estimation of the in-cylinder turbulence during the engine cycle based on a $K - k - \varepsilon$ 0D model. The use of this model showed that advancing the intake valve closing comes to degrade the level of turbulence at the end of the compression.

Further work on the methods and means to raise the level of the internal aerodynamics must still be conducted to ensure a positive impact from the use of the Miller cycle. However, it should also be noted that the global paradigm of the thermal engine is changing and that a decrease in turbulence would be beneficial for the use of fuels such as hydrogen, which has a laminar combustion speed that is already very high.

5. Conclusions and Future Works

This paper dealt with turbulence estimation during the compression stroke in the case of an EIVC Miller SI engine.

This evaluation was performed by comparing the PIV results with the numerical ones obtained from a RANS-type model. More precisely, the results of the 3D CFD numerical simulation were used to allow for the extrapolation of the data gathered through the PIV investigation toward the end of compression, where the PIV investigation did not provide information.

This paper also aimed to highlight that, despite the differences generated by a desirably perfect comparison between the experimental and numerical results, useful conclusions were extracted, as both approaches (CFD and PIV) offered comparable trends.

Thanks to this approach, the following values were obtained for the fluctuating velocity at 340° CA: 2.35 m s $^{-1}$ for the first VVT offset and 2.07 m s $^{-1}$ for the second. These values are considered low since, for the Otto case in the same configuration, the fluctuating velocity was of the order of 3.5 m s $^{-1}$, as shown in [17].

These findings support the conclusion that, when using the EIVC-based Miller cycle, special attention needs to be paid to the intensification of the internal aerodynamics of the engine in order to finally benefit from clean and efficient combustion. On this subject, beyond the solutions discussed in paper [15], one may imagine an intensification of the aerodynamic movement by using an asymmetric lift of the intake valves. The addition of a swirl component to the tumble movement stabilizes the general movement during the

compression phase. Another element that can be introduced as part of the optimization of the Miller cycle is the use of the engine at a high rpm to compensate for the loss of turbulent speed at the end of the compression.

However: (1) these findings are the consequences of working with the turbulent isotropic hypothesis, which was undertaken because only two velocity components can be measured with our PIV installation; the third component in the measurement plane could be obtained with a stereo PIV system [18], as presented in Section 2.1, meaning that a supplementary camera is needed; (2) the constants of the RANS model generally used for IC engine flow predictions were taken from the classical Otto cycle; this could lead to some inaccuracies when trying to predict the internal aerodynamics of a Miller cycle engine; (3) the blow-by flow mass estimated by the 0D approach (see Section 3.2) with its associated shortcomings, which was used as a boundary condition in the CFD simulation, could also lead to some imprecisions.

In light of these considerations, future works on this topic could be performed with a stereo PIV system and with a measurement of the blow-by flow mass. For the RANS-based CFD simulation, to study the influence of the RANS model constants on the predicted flow, parametric studies may be conducted. Another CFD approach would be to switch to LES with consideration of the boundary conditions well upstream of the intake ducts, which seems to deliver instantaneous velocity fields very close to the PIV results, as shown in papers [33,35,36]. Finally, another argument in favor of LES is that, since the RANS result is not the same average as the average of the PIV, an identical methodological approach would then impose the use of LES on as many cycles as possible so that the average is statistically converged.

Author Contributions: Conceptualization, P.G., A.C. and S.G.; methodology, M.P., P.G., A.C. and S.G.; PIV investigation, M.P.; CFD simulation, V.I.-S., M.N. and A.C.; writing—original draft preparation, M.P., A.C., M.N. and V.I.-S.; supervision, P.G., A.C. and S.G. All authors have read and agreed to the published version of the manuscript.

Funding: This research received no external funding.

Informed Consent Statement: Not applicable.

Data Availability Statement: Not applicable.

Acknowledgments: The authors want to express their gratitude to AVL List GmbH for providing the FIRE software for the CFD simulation.

Conflicts of Interest: The authors declare no conflict of interest.

Acronyms and Notations

0D	zero dimensional
3D	three dimensional
BC	boundary condition
BDC	bottom dead center
CA	crank angle
CFD	computational fluid dynamics
CPU	central processing unit
CO_2	carbon dioxide
EIVC	early intake valve closing
GB	gigabyte
GHz	gigahertz
IC	internal combustion
in/ex	intake/exhaust
LES	large eddy simulation
LIVC	late intake valve closing

MKE, K [$m^2 \cdot s^{-2}$]	mean kinetic energy
NO_x	nitrogen oxides
PIV	particle image velocimetry
RAM	random access memory
RANS	Reynolds-averaged Navier–Stokes
RDE	real driving emissions
rpm	revolutions per minute
RSM	Reynolds stress model
SI	spark ignition
TDC	top dead center
TKE, K [$m^2 \cdot s^{-2}$]	turbulent kinetic energy
URANS	unsteady Reynolds-averaged Navier–Stokes
VGT	variable geometry turbine
VVT	variable valve timing
A_{bb} [m^2]	leakage section/area
$\dot{m}_{th}$[kg/s]	blow-by mass flow rate
P_{cyl} [Pa]	in-cylinder pressure
P_{atm} [Pa]	atmospheric pressure
D_{cyl} [m]	bore
gap [m]	leakage gap
N_m	max. number of the grid's nodes
U_k [$m \cdot s^{-1}$]	*X* flow velocity at the *k* node
V_k [$m \cdot s^{-1}$]	*Y* flow velocity at the *k* node
u_i' [$m \cdot s^{-1}$]	velocity fluctuation of the *i* component
u_i [$m \cdot s^{-1}$]	velocity of the *i* component
$\overline{u}_i$ [$m \cdot s^{-1}$]	mean velocity of the *i* component
$k_{CFD/PIV}$ [$m^2 \cdot s^{-2}$]	mean TKE per mass unity for the CFD/PIV case
ζ	eddy viscosity
ε	rate of dissipation
ω	specific rate of dissipation
f	relaxation function
$v2$	velocity scale
g	the square root of a characteristic turbulent time scale

References

1. Miller, R. Miller cycle. Engine. U.S. Patent 2817322, 24 December 1957.
2. Mo, H.; Huang, Y.; Mao, X.; Zhuo, B. Investigations on the Potential of Miller Cycle for Performance Improvement of Gas Engine. *Glob. J. Res. Eng. B Automot. Eng.* **2016**, *16*, 36–46.
3. Braun, M.; Klaas, M.; Schröder, W. Influence of Miller Cycles on Engine Air Flow. *SAE Int. J. Engines* **2018**, *11*, 161–178. [CrossRef]
4. Huang, Z.-M.; Shen, K.; Wang, L.; Chen, W.-G.; Pan, J.-Y. Experimental study on the effects of the Miller cycle on the performance and emissions of a downsized turbocharged gasoline direct injection engine. *Adv. Mech. Eng.* **2020**, *12*, 1–9. [CrossRef]
5. Wang, Y.; Lin, L.; Zeng, S.; Huang, J.; Roskilly, A.P.; He, Y.; Huang, X.; Li, S. Application of the Miller cycle to reduce NOx emissions from petrol engines. *Appl. Energy* **2008**, *85*, 463–474. [CrossRef]
6. Transport & Environment. Road to Zero: The Last EU Emission Standard for Cars, Vans, Buses and Trucks. 2020. Available online: https://www.transportenvironment.org/wp-content/uploads/2021/06/2020_04_Road_to_Zero_last_EU_emission_standard_cars_vans_buses_trucks.pdf (accessed on 16 March 2022).
7. Budack, R.; Wurms, R.; Mendl, G.; Heiduk, T. The New Audi 2.0-l I4 TFSI Engine. *MTZ Worldw.* **2016**, *77*, 16–23. [CrossRef]
8. Demmelbauer-Ebner, W.; Persigehl, K.; Görke, M.; Werstat, E. The New 1.5-l Four-cylinder TSI Engine from Volkswagen. *MTZ Worldw.* **2017**, *78*, 16–23. [CrossRef]
9. Demmelbauer-Ebner, W.; Theobald, J.; Worm, J.; Scheller, P. The new 1.5-l EA211 TGI evo. *MTZ Worldw.* **2018**, *79*, 16–21. [CrossRef]
10. European Automobile Manufacturers Association. What Is the Real Driving Emissions (RDE) Test? Car Emissions Testing Facts. 2018. Available online: http://www.caremissionstestingfacts.eu/rde-real-driving-emissions-test/ (accessed on 17 March 2022).
11. Nose, H.; Inoue, T.; Katagiri, S.; Sakai, A.; Kawasaki, T.; Okamura, M. Fuel Enrichment Control System by Catalyst Temperature Estimation to Enable Frequent Stoichiometric Operation at High Engine Speed/Load Condition. In Proceedings of the SAE 2013 World Congress & Exhibition, Detroit, MI, USA, 16–18 April 2013; pp. 16–18. [CrossRef]
12. Morand, N.; Agnew, G.; Bontemps, N.; Jeckel, D. Variable Nozzle Turbine Turbocharger for Gasoline 'Miller' Engine. *MTZ Worldw.* **2016**, *78*, 40–45. [CrossRef]

13. Penzel, M.; Bevilacqua, V.; Böger, M. Meeting Future Emission Standards with Turbocharged High-Performance Gasoline Engines. *MTZ Worldw.* **2020**, *81*, 16–25. [CrossRef]
14. Scheidt, I.M.; Brands, I.C.; Kratzsch, M.; Günther, M. Combined Miller/Atkinson Strategy for Future Downsizing Concepts. *MTZ Worldw.* **2014**, *75*, 4–11. [CrossRef]
15. Niculae, M.; Clenci, A.; Iorga-Simăn, V.; Niculescu, R. Évaluation de l'impact du masquage des soupapes d'admission et de l'augmentation de la course du piston sur l'aérodynamique interne du moteur Miller. *Entropie Thermodyn. Énergie Environ. Économie* **2021**, *1*. [CrossRef]
16. Xu, J.; Guo, T.; Feng, Y.; Sun, M. Numerical investigation of Miller cycle with EIVC and LIVC on a high compression ratio gasoline engine. *Sci. Prog.* **2021**, *104*, 368504211023640. [CrossRef] [PubMed]
17. Cao, Y. Sensibilité d'un Ecoulement de Rouleau Compressé et des Variations Cycle à Cycle Associées à des Paramètres de Remplissage Moteur. Ph.D. Thesis, ENSMA, Chasseneuil-du-Poitou, France, 2014.
18. El-Adawy, M.; Heikal, M.; Aziz, A.R.A.; Opatola, R.A. Stereoscopic particle image velocimetry for engine flow measurements: Principles and applications. *Alex. Eng. J.* **2021**, *60*, 3327–3344. [CrossRef]
19. Matsuda, M.; Yokomori, T.; Shimura, M.; Minamoto, Y.; Tanahashi, M.; Iida, N. Development of cycle-to-cycle variation of the tumble flow motion in a cylinder of a spark ignition internal combustion engine with Miller cycle. *Int. J. Engine Res.* **2020**, *22*, 1512–1524. [CrossRef]
20. EBaum, E.; Peterson, B.; Surmann, C.; Michaelis, D.; Böhm, B.; Dreizler, A. Tomographic PIV measurements in an IC engine. In Proceedings of the 16th International Symposium on Applications of Laser Techniques to Fluid Mechanics Conference, Lisbon, Portugal, 16–19 July 2012; pp. 1–12.
21. Lee, H. Thermographic PIV for Turbulent Flux Measurement. Technische Universität Darmstadt. 2016. Available online: https://tuprints.ulb.tu-darmstadt.de/5532/ (accessed on 18 March 2022).
22. Jahanmiri, M. Particle Image Velocimetry: Fundamentals and Its Applications. Goteborg. 2011. Available online: https://www.academia.edu/2263312/Particle_Image_Velocimetry_Fundamentals_and_Its_Applications (accessed on 18 March 2022).
23. Lawson, J.M.; Dawson, J.R. A scanning PIV method for fine-scale turbulence measurements. *Exp. Fluids* **2014**, *55*, 1857. [CrossRef]
24. Adrian, R.J. Measurement Potential of Laser Speckle Velocimetry. NASA Conference Publication. October 1982. Available online: https://www.researchgate.net/publication/4675662_Measurement_potential_of_laser_speckle_velocimetry (accessed on 19 March 2022).
25. Koochesfahani, M.M.; Nocera, D.G. Molecular Tagging Velocimetry. In *Springer Handbook of Experimental Fluid Mechanics*; Tropea, H.C., Yarin, A., Foss, J.F., Eds.; Springer: Berlin/Heidelberg, Germany, 2007. [CrossRef]
26. Meier, A.H.; Roesgen, T. Imaging laser Doppler velocimetry. *Exp. Fluids* **2011**, *52*, 1017–1026. [CrossRef]
27. Hanjalić, K.; Popovac, M.; Hadžiabdić, M. A robust near-wall elliptic-relaxation eddy-viscosity turbulence model for CFD. *Int. J. Heat Fluid Flow* **2004**, *25*, 1047–1051. [CrossRef]
28. Basara, B. Analysis of the performance of linear and non-linear K-ε-ζ-F turbulence model on various applications. In Proceedings of the Fluids Engineering Division Summer Meeting, Miami, FL, USA, 17–20 July 2006; pp. 239–247. [CrossRef]
29. Alfonsi, G. Reynolds-Averaged Navier–Stokes Equations for Turbulence Modeling. *Appl. Mech. Rev.* **2009**, *62*, 040802. [CrossRef]
30. Yang, X.; Gupta, S.; Kuo, T.-W.; Gopalakrishnan, V. RANS and large Eddy simulation of internal combustion engine flows—A comparative study. *J. Eng. Gas Turbines Power* **2014**, *136*, 051507. [CrossRef]
31. Hasse, C.; Sohm, V.; Durst, B. Numerical investigation of cyclic variations in gasoline engines using a hybrid URANS/LES modeling approach. *Comput. Fluids* **2009**, *39*, 25–48. [CrossRef]
32. Hasse, C.; Sohm, V.; Durst, B. Detached eddy simulation of cyclic large scale fluctuations in a simplified engine setup. *Int. J. Heat Fluid Flow* **2009**, *30*, 32–43. [CrossRef]
33. SBuhl, S.; Dietzsch, F.; Buhl, C.; Hasse, C. Comparative study of turbulence models for scale-resolving simulations of internal combustion engine flows. *Comput. Fluids* **2017**, *156*, 66–80. [CrossRef]
34. Hemmingsen, C.S.; Ingvorsen, K.M.; Mayer, S.; Walther, J.H. LES And URANS simulations of the swirling flow in a dynamic model of a uniflow-scavenged cylinder. *Int. J. Heat Fluid Flow* **2016**, *62*, 213–223. [CrossRef]
35. Krastev, V.; Di Ilio, G.; Falcucci, G.; Bella, G. Notes on the hybrid URANS/LES turbulence modeling for Internal Combustion Engines simulation. *Energy Procedia* **2018**, *148*, 1098–1104. [CrossRef]
36. Enaux, B.; Granet, V.; Vermorel, O.; Lacour, C.; Thobois, L.; Dugué, V.; Poinsot, T. Large Eddy Simulation of a Motored Single-Cylinder Piston Engine: Numerical Strategies and Validation. *Flow Turbul. Combust.* **2010**, *86*, 153–177. [CrossRef]
37. Bakker, A. Lectures on Applied Computational Fluid Dynamics. Dartmouth College. 2008. Available online: https://www.bakker.org/Lectures-Applied-CFD.pdf (accessed on 15 January 2020).
38. Krastev, V.K.; Silvestri, L.; Falcucci, G.; Bella, G. A Zonal-LES Study of Steady and Reciprocating Engine-Like Flows Using a Modified Two-Equation des Turbulence Model. *SAE Technical Paper*, September 2017. [CrossRef]
39. Krastev, V.; Silvestri, L.; Bella, G. Effects of Turbulence Modeling and Grid Quality on the Zonal URANS/LES Simulation of Static and Reciprocating Engine-Like Geometries. *SAE Int. J. Engines* **2018**, *11*, 669–686. [CrossRef]
40. Karbon, M.; Sleiti, A.K. Turbulence Modeling Using Z-F Model and RSM for Flow Analysis in Z-SHAPE Ducts. *J. Eng.* **2020**, *2020*, 4854837. [CrossRef]
41. Durbin, P.A. Near-Wall Turbulence Closure Modeling without "Damping Functions". *Theor. Comput. Fluid Dyn.* **1991**, *3*, 1–13. [CrossRef]

42. Advanced Simulation Technologies. In *AVL FIRE—Turbulence Modeling (Brochure)*; AVL List GmbH: Graz, Austria, 2009.
43. Perceau, M.; Guibert, P.; Guilain, S. Zero-dimensional turbulence modeling of a spark ignition engine in a Miller cycle «Dethrottling» approach using a variable valve timing system. *Appl. Therm. Eng.* **2021**, *199*, 117535. [CrossRef]
44. Kirkpatrick, A.T.; Ferguson, C.R. *Internal Combustion Engines*, 3rd ed.; Wiley: Hoboken, NJ, USA, 2016. [CrossRef]